Structure of a hard-sphere fluid in hard wedges

M. Schoen*
Institut für Theoretische Physik, Sekretariat PN 7-1, Fachbereich Physik, Technische Universität Berlin, Hardenbergstraße 36, D-10623 Berlin, Germany

S. Dietrich†
Fachbereich Physik, Bergische Universität Wuppertal, D-42097 Wuppertal, Germany
(Received 12 February 1997)

We investigate local structural properties of a hard-sphere fluid exposed to periodic arrays of parallel hard wedges by means of grand canonical ensemble Monte Carlo simulations. The corrugated substrate is characterized by the dihedral angle γ of the grooves, the angle $2\pi-\gamma$ of the tips, and the lateral periodicity length s_x in the x direction; γ is varied over the range $\pi/2\leqslant\gamma\leqslant\pi$ including a planar wall ($\gamma=\pi$) as a special case. In the second lateral direction y periodic boundary conditions are used, whereas confinement in the normal direction z is accomplished by two opposite substrates sufficiently far apart. We analyze the ordering of the fluid within the grooves and at the tips, respectively, in terms of the number density $\rho(x,z;\gamma)$. The crossover between these two regions exhibits pronounced density oscillations. From the density distribution we extract the excess coverage $\Gamma(\gamma)$, which up to now has been known only for $\gamma=\pi$; in this special case we find excellent agreement with previous work. $\Gamma(\gamma)$ is composed of surface and line contribution whose relative magnitude permits us to quantify corrugation effects vs planar confinement. [S1063-651X(97)10507-4]

PACS number(s): 61.20.Ja, 61.20.Ne, 68.45.−v

I. INTRODUCTION

Confinement of a fluid by container walls imposes spatial inhomogeneities in the fluid. They range from packing effects close to the walls [1,2], which cause the local density to be a strongly oscillatory function of position, to quasimacroscopic effects such as wetting [3–7]. Experimentally these effects are accessible by scattering of light [8], x rays, and neutrons [9,10] as well as by force microscopy [11–14]. In the vast majority of corresponding theoretical studies, the walls are modeled by substrate potentials which vary only in the direction normal to the surface, but are translationally invariant in lateral directions. However, even for atomically flat substrates this is an oversimplification because of the actual atomic corrugation of the substrate.

Unless substrates have been treated with great care, they are typically rough, so that an adjacent fluid is exposed to a geometrically disordered wall. The effect of such disorder on wetting phenomena has been studied experimentally [15–18] and theoretically [19–22] by coarse-grained approaches which average laterally over the local height variation of the substrate. Thus an understanding of the *local* microscopic structure of fluids filling the grooves and covering the tips of such disordered substrates is not yet available.

This dearth of information is aggravated by the fact that it became possible to prepare substrates which exhibit well-defined geometric structures with lateral periodicity in one direction. X-ray scattering provides spatially resolved density distributions of fluids in contact with such substrates [23]. The first steps in understanding the wetting of single wedges were made, but they focused on the shape of the meniscus forming inside the grooves [24]. Therefore, these studies do not address packing effects occurring in a fluid when its confining walls start to interfere upon approaching the center of a wedge or when they form a tip. Such effects are important in the context of microfluidity, where one follows the spreading of liquids in artificial grooves [25–27]. At the surfaces of certain materials grooves may even form spontaneously. One may encounter situations in which planar terraces of molecularly large areas are separated by steps of a height of several atomic layers. Such structures can be quite regular even in natural materials. For instance, minerals of the palygorskite and sepiolite group consist of stacks of alternating tetrahedral and octahedral silicate sheets [28]. The structure and diffusion of ''simple'' fluids in grooves of this particular geometry were recently investigated by computer simulation methods [29].

To promote a more detailed understanding of fluid structures caused by geometrical confinement, we analyze a hard-sphere fluid exposed to a periodic array of wedges. In this model attractive forces between fluid particles and with the substrate are absent, and the repulsive part of the interactions is replaced by hard cores. This permits one to isolate the purely entropic effects of spatial confinements on fluid structure. Since short-ranged order in fluids is dominated by packing effects the present results also provide important insight into the behavior of fluids endowed with more realistic interaction potentials. Moreover, the hard-sphere fluid represents a convenient starting point for analytic theories so that the present results provide a benchmark for future density-functional calculations of such systems. Finally, we would like to mention that by suitable choices of wall, solute, and solvent, the present model of hard spheres in hard grooves can closely resemble a colloidal suspension in which the colloidal particles behave effectively as hard spheres. Therefore, the results of the present Monte Carlo calculations are

*Electronic address: M.Schoen@physik.tu-berlin.de
†Electronic address: dietrich@wptsb.physik.uni-wuppertal.de

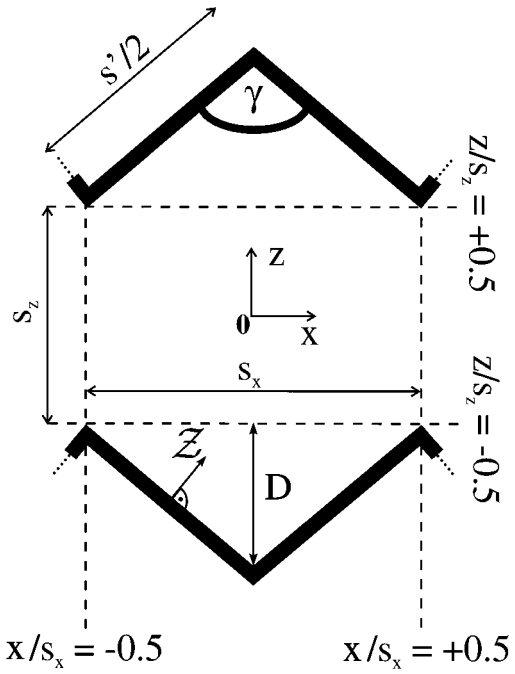

FIG. 1. Side view of the model system consisting of two opposite hard wedges of side length s' and dihedral angle γ in the (x,z) plane. The origin **0** of the coordinate system is at the center, halfway in between the wedges. The corner of the wedge is located at $x/s_x=0$ and the two tips at $x/s_x=\pm 0.5$ are separated by a distance s_z along the z axis of the coordinate system. Also shown is a point at a distance $\mathcal{Z}$ in a direction normal to a wedge wall. The system is periodically extended in the x direction with a unit length s_x. The depth of a wedges is denoted by D.

also accessible to experimental tests.

In Sec. II we present our model and discuss numerical aspects of the simulations. Results are analyzed in Sec. III, and summarized in Sec. IV.

II. NUMERICAL ASPECTS

A. Monte Carlo simulations in the grand canonical ensemble

In Fig. 1 we sketch our model system consisting of two opposing wedges characterized by their dihedral angle γ and the lateral width s_x. Tips at $|x|/s_x=0.5$ are separated by a distance s_z along the z axis of the coordinate system fixed at the center **0**. For sufficiently large values of s_z, this system reduces to two identical, independent interfaces between the fluid and the corrugated substrate separated by the bulk fluid. The angle γ and the fixed side length $s'/2$ determine the lateral width s_x:

$$\frac{s_x}{2}=\frac{s'}{2}\sin(\gamma/2). \tag{1}$$

The system is therefore symmetric with respect to $x-y$ and $z-y$ planes (cf. Sec. II B). We employ periodic boundary conditions [30] in x and y directions at planes $x=\pm s_x/2$ and $y=\pm s'/2$. Therefore, the walls of our system represent a sawtooth-shaped, corrugated substrate. The depth of each groove is given by $D=(s_x/2)\cot(\gamma/2)$, so that in the limit of large s_x one recovers the single-wedge model [24].

In order to describe the fluid in this confined geometry we resort to the grand canonical ensemble in which a thermodynamic state is uniquely specified by chemical potential μ, volume V, and temperature T. Because of the spatially inhomogeneous density distribution, the canonical ensemble with its specification of the averaged mean density is a less favorable choice. Ensemble averages $\langle O\rangle$ of an observable O can be expressed as [31]

$$\langle O\rangle=\Xi^{-1}\sum_{N=0}^{\infty}(\Lambda^{3N}N!)^{-1}\int_{V^N}d\boldsymbol{r}^N O(\boldsymbol{r}^N)\exp[-\beta U(\boldsymbol{r}^N)]$$

$$=\sum_{N=0}^{\infty}\int_{V^N}d\boldsymbol{r}^N O(\boldsymbol{r}^N)f_{\mu VT} \tag{2}$$

in the classical limit. In Eq. (2), Ξ is the grand canonical partition function, Λ is the thermal de Broglie wavelength [31], $\beta:=(k_BT)^{-1}$ (k_B Boltzmann's constant), $\boldsymbol{r}^N$ is an abbreviation for the set (i.e., the configuration) $\{\boldsymbol{r}_1,\boldsymbol{r}_2,\ldots,\boldsymbol{r}_N\}$, U is the configurational energy, and $O(\boldsymbol{r}^N)$ is a molecular representation of the quantity of interest which may depend on additional external variables. In the present context we focus on

$$O(\boldsymbol{r}',\boldsymbol{r}^N)=\sum_{i=1}^{N}\delta(\boldsymbol{r}_i-\boldsymbol{r}') \tag{3}$$

because $\langle O(\boldsymbol{r}')\rangle=\rho(\boldsymbol{r}')$ is the local (number) density $\rho(\boldsymbol{r}')$ of the fluid. In Eq. (3), δ is the Dirac δ function. In Eq. (2) we assume that the fluid is composed of spherically symmetric particles, so that their configuration is uniquely characterized by the set of coordinates of their centers.

In order to determine $\rho(\boldsymbol{r}')$ we resort to grand canonical ensemble Monte Carlo (GCEMC) simulations. In GCEMC the generation of a (numerical representation of) a Markov chain of configurations proceeds in two consecutive steps. In the first step one of the N spheres, say i, is chosen at random and displaced slightly within a small cube of side length $2d_{\max}$ centered at its original position $\boldsymbol{r}_i^{[k]}$; that is

$$\boldsymbol{r}_i^{[l]}=\boldsymbol{r}_i^{[k]}+d_{\max}(\mathbf{1}-2\boldsymbol{\xi}), \tag{4}$$

where superscripts refer to original $[k]$ and new trial configurations $[l]$, $\mathbf{1}=(1,1,1)$, and $\boldsymbol{\xi}$ is a vector whose three dimensionless components are pseudorandom numbers distributed uniformly on the interval $[0,1]$. The parameter $d_{\max}$ is adjusted during a run to preserve an overall acceptance ratio of 40–60 % of all displacement attempts. From the theory of Markov processes [32] it follows that the probability of acceptance of the transition $k\to l$ is governed by the ratio $f_{\mu VT}^{[l]}/f_{\mu VT}^{[k]}$ [see Eq. (2)], where

$$f_{\mu VT}\propto\exp[-\beta(U-\mu N)-\ln N!-N\ln(\Lambda^3/V)]. \tag{5}$$

Since N does not vary during the first step, it is easy to verify that

$$\frac{f_{\mu VT}^{[l]}}{f_{\mu VT}^{[k]}}=\exp[-\beta\Delta U_{k\to l}], \tag{6}$$

where $\Delta U_{k\to l}$ is the change in configurational energy associated with the displacement of sphere i. Because of the infinitely repulsive fluid-fluid pair and substrate potentials, one has

$$\Delta U_{k\to l}=0 \quad \text{if} \quad r_{ij}>\sigma, \quad 1\leqslant i\neq j\leqslant N \quad \text{and} \quad |z_i|\leqslant z_{\text{wall}}(x_i;\gamma), \quad 1\leqslant i\leqslant N, \tag{7}$$

where

$$z_{\text{wall}}(x;\gamma)=\left(\frac{s_x}{2}-x\right)\cot\left(\frac{\gamma}{2}\right)+\frac{s_z}{2}-\frac{\sigma}{\sin(\gamma/2)}, \quad |x|\leqslant\frac{s_x}{2} \tag{8}$$

is the position of closest contact of the centers of the spheres with the wall, $r_{ij}=[(x_i-x_j)^2+(y_i-y_j)^2+(z_i-z_j)^2]^{1/2}$ is the distance between the centers of any pair of hard spheres, and σ is the hard-sphere diameter. If the wall is thought of as being composed of fixed hard spheres of the same diameter σ, $z_{\text{wall}}(x;\gamma)+\sigma/\sin(\gamma/2)$ is the position of the centers of the substrate spheres in the top layer of the substrate; this gives rise to the last term in Eq. (8). If the displacement of sphere i violates one or both of the two conditions stated in Eq. (7), one has $\Delta U_{k\to l}=\infty$. Employing Metropolis' algorithm [30] the transition $k\to l$ is either accepted with probability $p=1$ $(\Delta U_{k\to l}=0)$ or rejected $(p=0,\Delta U_{k\to l}=\infty)$.

During the second step an attempt is made to alter N by either adding or removing one hard sphere in an unbiased way; that is, addition and removal are attempted with equal probability. If $\Delta N_{k\to l}:=N^{[l]}-N^{[k]}=+1$, a new hard sphere is added from a virtual reservoir of matter at a randomly determined position in V; if $\Delta N_{k\to l}=-1$, an already existing sphere is chosen at random and subjected to a removal attempt. Addition and removal are governed by [see Eq. (5)]

$$\frac{f^{[l]}_{\mu VT}}{f^{[k]}_{\mu VT}}=\exp(r_{k\to l}), \tag{9}$$

where for an addition attempt the argument of the pseudo-Boltzmann factor is given by

$$r_{k\to l}=-\ln N^{[l]}+B \quad \text{if} \quad r_{ij}>\sigma, \quad 1\leqslant i\neq j\leqslant N \quad \text{and} \quad |z_i|\leqslant z_{\text{wall}}(x;\gamma), \quad 1\leqslant i\leqslant N \tag{10}$$

because $U^{[l]}=0$ under these conditions; if one or both of these conditions are violated $U^{[l]}=\infty$ and $r_{k\to l}=-\infty$ so that addition is rejected without further ado. For a removal attempt,

$$r_{k\to l}=\ln N^{[k]}-B, \tag{11}$$

because $U^{[k]}=0$ in any event (i.e., $U^{[k]}$ vanishes *by definition* for each of the N hard spheres in *all* configurations of the Markov chain). The quantity B in Eqs. (10) and (11), which is a dimensionless number, is related to the chemical potential via

$$B=\beta\mu-\ln(\Lambda^3/V)=C+\ln(V/\sigma^3). \tag{12}$$

Its introduction is convenient from a purely technical perspective of the simulations as demonstrated by Adams [33]. In the same spirit we introduce the dimensionless number C which is fixed throughout this paper (see Sec. II B below). Both addition (for configurations characterized by a finite $r_{k\to l}$, i.e., $U^{[l]}=0$) and removal attempts are accepted with probability

$$p=\min[1,\exp(r_{k\to l})] \tag{13}$$

by comparing the pseudo-Boltzmann factor with a random number ξ uniformly distributed on the interval $[1,0]$ [30].

B. Reliability of the computational scheme

The GCEMC algorithm just described was subjected to a number of consistency checks. Throughout this paper we focus exclusively on a thermodynamic state characterized by $C=7.056$ [see Eq. (12)], corresponding to an average density of a hard-sphere bulk fluid of $\rho_b\sigma^3:=\rho_b^*=0.7016$ obtained from GCEMC simulations. Because of the simple form of the interaction potential, some properties of the hard-sphere fluid are amenable to approximate analytic analyses. For example, the Carnahan-Starling (CS) equation of state [34] expresses the pressure P_{CS} in a bulk hard-sphere fluid

$$\frac{\beta P_{\text{CS}}}{\rho_b}=\frac{1+\eta+\eta^2-\eta^3}{(1-\eta)^3} \tag{14}$$

in terms of the hard-sphere packing fraction $\eta:=\pi\rho_b^*/6$, so that $\beta P_{\text{CS}}/\sigma^3=P_{\text{CS}}^*=4.026$ for the present choice. Furthermore, the pressure of a bulk hard-sphere fluid is related to the contact value of its radial pair correlation function $g(r)$ via [31]

$$\frac{\beta P}{\rho_b}=1+\frac{2\pi}{3}\rho_b\sigma^3\lim_{r\to\sigma^+}g(r). \tag{15}$$

It can be determined in GCEMC simulations from the relation

$$g(r)=\frac{\langle N(r)\rangle}{4\pi\overline{\rho_b}r^2\Delta r}, \tag{16}$$

which is normalized such that $g(r\to\infty)=1$. In Eq. (16), $\langle N(r)\rangle$ denotes the average number of hard spheres located in a spherical shell of thickness Δr separated from a reference sphere at the origin by a distance r. The overbar is used to emphasize that $\overline{\rho_b}$ in the denominator of Eq. (16) is averaged over the Markov chain generated according to Sec. II A. Averages involve a few thousand statistically uncorrelated configurations in which each sphere serves as a reference. For the present value of C we obtain a contact value $g(\sigma^+)=3.2315$. According to Eq. (15) this yields $P^*=4.033$, in very good agreement with $P_{\text{CS}}^*=4.026$.

An additional check is provided by decomposing the free energy of the hard-sphere fluid into two terms,

$$F=F^{\text{id}}+F^{\text{ex}}, \tag{17}$$

where the ideal-gas part is given by [35]

$$\frac{\beta F^{\text{id}}}{N}=\ln(\rho_b\sigma^3)+3\ln(\Lambda/\sigma)-1 \tag{18}$$

and the excess part by [35]

$$\frac{\beta F^{\mathrm{ex}}}{N}=\int_0^{\eta}\left[\frac{\beta P_{\mathrm{CS}}(\eta')}{\rho_b}-1\right]d\,\ln\eta'=\frac{\eta(4-3\eta)}{(1-\eta)^2}. \quad (19)$$

Equations (17)–(19) together with the thermodynamic relation

$$\mu=\left(\frac{\partial F}{\partial N}\right)_{T,V} \quad (20)$$

allow one to express μ in terms of the hard-sphere packing fraction

$$\mu=\mu^{\mathrm{id}}+\mu^{\mathrm{ex}},$$

$$\beta\mu^{\mathrm{id}}=\ln(\rho_b\sigma^3)+3\ln(\Lambda/\sigma), \quad (21)$$

$$\beta\mu^{\mathrm{ex}}=\frac{8\eta-9\eta^2+3\eta^3}{(1-\eta)^3}.$$

For our present choice of $C=7.056$ [see Eq. (12)] we obtain $\rho_b^*=0.7016$ from GCEMC simulations, so that $C-\ln\rho_b^*=\beta\mu^{\mathrm{ex}}=7.410$, in excellent agreement with $\beta\mu^{\mathrm{ex}}=7.397$ calculated directly from the third expression in Eq. (21) for the same density.

After passing these consistency checks in the bulk we now turn to the local number density

$$\rho(x,z;\gamma):=\frac{\langle N(x,z;\gamma)\rangle}{s'\,\delta x\,\delta z} \quad (22)$$

describing the microscopic fluid structure in the geometry shown in Fig. 1. For a given configuration, $\langle N(x,z;\gamma)\rangle$ is the average number of hard spheres whose centers are contained in a small parallelepiped of volume $s'\delta x\delta z$ centered at a point (x,z) and adapted to the wedge geometry (see Fig. 1). In the special case of planar walls ($\gamma=\pi$) the local number density is independent of x so that

$$\rho(z)=\frac{1}{s'}\int_{-s'/2}^{s'/2}dx\;\rho(x,z;\pi)=\frac{\langle N(z)\rangle}{A\,\delta z}, \quad (23)$$

where the limits of integration follow from Eq. (1) and our choice of the coordinate system (see Fig. 1). The far right-hand side of Eq. (23) states explicitly the numerical recipe for a direct computation of $\rho(z)$ in GCEMC simulations, where $\langle N(z)\rangle$ is the average number of hard spheres whose centers are contained in a thin slice of thickness δz centered at z and parallel to the (planar) walls of area $A=s'^2$. In this planar limit one has the rigorous relation

$$\beta P=\lim_{z\to z_{\mathrm{wall}}(x;\gamma)+0}\rho(z) \quad (24)$$

known as the ''wall theorem'' [14]. From $\rho(z)$ shown in Fig. 2, for our present system we obtain $P^*=3.972$, which agrees nicely with $P_{\mathrm{CS}}^*=4.026$ and $P^*=4.033$ following from Eq. (15). In the thermodynamic limit $s'\to\infty$ one has

$$\lim_{z\to\infty}\rho(x,z;\gamma)=\rho_b, \quad (25)$$

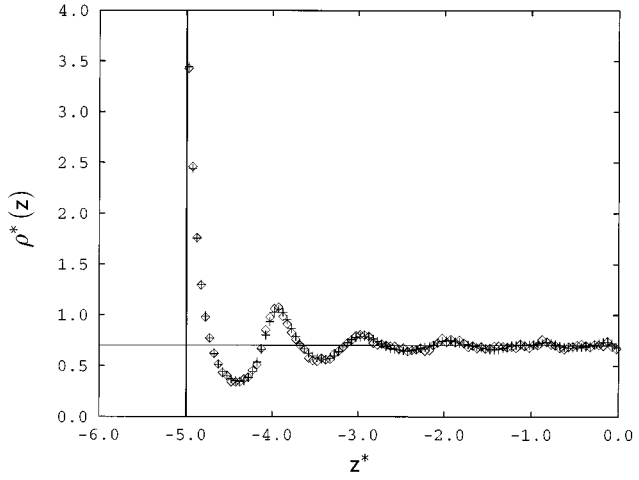

FIG. 2. The local number density $\rho^*(z)=\rho(z)\sigma^3$ [see Eq. (23)] of a hard-sphere fluid confined by two planar walls (in view of the symmetry of the system data are presented only for the lower half of the system $z/s_z\leq 0.0$; see Fig. 1) as a function of the normal distance $z^*=z\sigma^{-1}$ ($\diamond$) for $s_z^*=s_z\sigma^{-1}=12$. The positions of the nuclei of the top layer of the lower substrate is given by $z^*=-6$ so that for $z^*<-5$ (indicated by the vertical line) $\rho^*(z)=0$. Extrapolation of $\rho^*(z)$ to $z^*\to-5$ yields the value 3.972. For comparison we also show a cut $\rho(x=\mathrm{const},z;\pi)$ [see Eq. (22)] along an arbitrarily selected line $x^*=4.075$ after the corresponding density profile was smoothed appropriately (see Sec. III A) (+). The horizontal line indicates the bulk density $\rho_b^*=0.7016$.

irrespective of x and γ. The plot in Fig. 2 shows agreement with this relation within numerical accuracy for the special case $\gamma=\pi$ (for other angles γ, see below), $s_z^*=12.0$ and $s'^*=10.0$ for which all the results below are obtained. Thus we conclude that a distance of $s_z^*=12.0$ is sufficiently large so that the local fluid structure in the vicinity of one wall is unperturbed by the presence of the opposite one (see Fig. 1) in agreement with density-functional results [36].

III. RESULTS

A. Data smoothing

In GCEMC numerical complications arise in the calculation of $\rho(x,z;\gamma)$ via Eq. (22) because for small values of γ and close to a wedge corner ($|x|\lesssim\sigma$) $\rho(x,z;\gamma)$ varies rapidly. This requires a very fine resolution $\delta x^*=\delta z^*=0.05$ of the histogram [see Eq. (22)] in order to resolve details of local fluid structure in this regime. However, employing such a fine-meshed grid causes poor statistics even for very long GCEMC runs of 5×10^8 steps which we have used predominantly. These simulations take approximately four days of CPU time on a DEC Alpha workstation. Statistical accuracy can be enhanced modestly by averaging the data over the four geometrically equivalent quadrants ($x\geq0,z\geq0$), ($x\leq0,z\geq0$), ($x\geq0,z\leq0$), and ($x\leq0,z\leq0$). The remaining statistical fluctuations are still significant as illustrated for a representative case in Fig. 3(a), where $\rho(x,z;\gamma=\pi)$ is plotted. The plot demonstrates that statistical fluctuations are particularly pronounced far away from the walls where the fluid is less structured. To facilitate an analysis of such noisy simulation data we apply a least-squares smoothing proce-

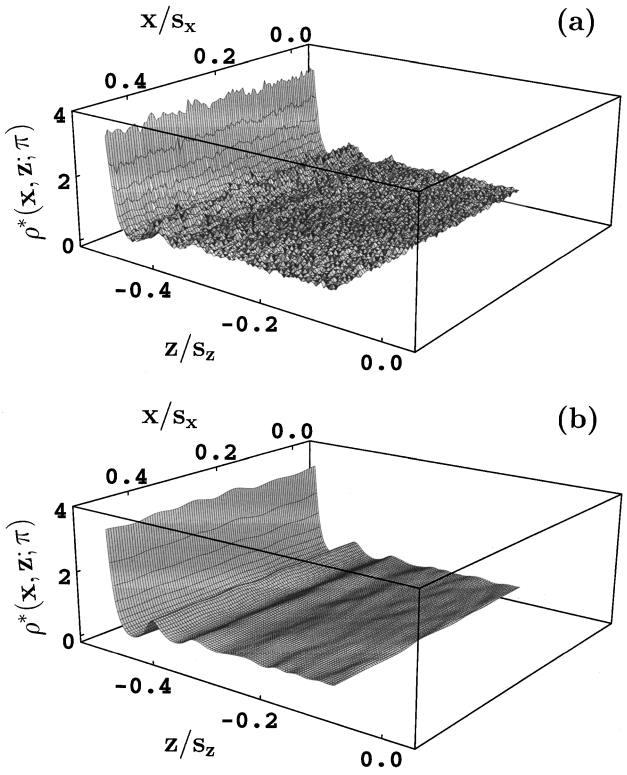

FIG. 3. The number density profile $\rho^*(x,z;\gamma=\pi)$ [see Eq. (22)] of a hard-sphere fluid confined by two planar walls at a distance $s_z^*=s_z\sigma^{-1}=12$ (only the lower half of the system is shown) as a function of lateral x/s_x and normal position z/s_z before smoothing (a) and after smoothing (b) (see Sec. III A).

dure which removes the statistical noise without affecting physically relevant features of $\rho(x,z;\gamma)$.

Since physically relevant variations of $\rho(x,z;\gamma)$ are least parallel to the walls it is advantageous to transform variables according to $(x,z)\rightarrow[x,\Delta z=z-z_{\rm wall}(x;\gamma)]$ prior to smoothing. By fitting a quadratic polynomial locally to five equally spaced data points $\rho_k=\rho(x_k,\Delta z=\text{const};\gamma)$, it can be shown [37] that the value of the polynomial at the midpoint corresponds to a ''smoothed'' value of $\rho(x,\Delta z;\gamma)$ at this point. This value is obtained from the so-called normal equations which lead to an expression [37]

$$\rho_k^{[l]}=\rho_k^{[l-1]}-\tfrac{3}{35}(\Delta x)^4\Delta_{k-2}^{(4),[l-1]},\quad k=1,\ldots,n_x, \tag{26}$$

where n_x is the number of histogram entries in the x direction, and the superscript $l=1,\ldots,l_{\rm max}$ labels the smoothing cycle which is carried out iteratively $l_{\rm max}$ times (see below). The quantity

$$\Delta_k^{(4),[l]}:=\frac{1}{(\Delta x)^4}(\rho_{k-2}^{[l]}-4\rho_{k-1}^{[l]}+6\rho_k^{[l]}-4\rho_{k+1}^{[l]}+\rho_{k+2}^{[l]}) \tag{27}$$

corresponds to the fourth derivative of $\rho(x,z;\gamma)$ at the point x_k and for the lth smoothing cycle. At the boundaries we employ the periodicity of the system and set $\rho_0^{[l-1]}=\rho_2^{[l-1]}$, $\rho_{-1}^{[l-1]}=\rho_3^{[l-1]}$, $\rho_{-2}^{[l-1]}=\rho_4^{[l-1]}$, and $\rho_{-3}^{[l-1]}=\rho_5^{[l-1]}$. In practice one observes that ρ_k changes significantly only during first few iterations, in which most of the statistical noise is eliminated. The density profile is remarkably robust with respect to further iterations so that within reasonable limits the precise number of iterations $l_{\rm max}$ does not matter very much. Data presented below are typically based on $l_{\rm max}=O(10-100)$. Once $l_{\rm max}$ has been reached, smoothing is repeated in the fashion just described for the next cut $\Delta z+\delta z=\text{const}$, until all the $j=1,\ldots,n_z$ cuts are processed where n_z denotes the number of histogram entries in the z direction along a line $x=\text{const}$.

To demonstrate the reliability of this procedure, we apply it to the raw simulation data plotted in Fig. 3(a). The resulting smoothed profile is shown in Fig. 3(b). For an arbitrary cut $x=\text{const}$, in Fig. 2 we compare $\rho(x=\text{const},z;\gamma=\pi)$ obtained from Eq. (22) after smoothing with $\rho(z)$ obtained from the far right-hand side of Eq. (23). After 10^8 GCEMC steps, $\rho(z)$ turns out to be fairly smooth. The plots in Fig. 2 also show that $\rho(z)$ agrees nicely with $\rho(x=\text{const},z;\gamma=\pi)$ especially as far as the contact value, i.e., the pressure [see Eq. (24)] is concerned. Heights and positions of higher-order peaks (i.e., peaks at larger distances from the wall) remain also unaffected by smoothing. Furthermore, at sufficiently large distances from the wall the smoothed curve attains its limiting value ρ_b within statistical errors. Therefore, we conclude that smoothing as outlined in this subsection does not alter physically significant structures of density profiles, but serves to eliminate irrelevant statistical noise from raw GCEMC data conveniently and satisfactorily. Thus, in the remainder of this paper, only smoothed profiles will be presented and discussed.

B. Local-density distribution

The effects of substrate corrugation are conveniently expressed in terms of the deviation of the local density in a wedge of dihedral angle γ from the corresponding one at a planar wall at the same distance $\mathcal{Z}$ (see Fig. 1) from that wall,

$$\Delta\rho(x,\Delta z;\gamma):=\rho(x,\Delta z;\gamma)-\rho(x,\mathcal{Z};\gamma=\pi). \tag{28}$$

This is shown in Fig. 4 for four selected dihedral angles γ; for reasons of clarity the original variables x and z are used in these plots. For $\gamma=8\pi/9$ the substrate is almost planar, so that $\Delta\rho$ vanishes nearly everywhere except in the close vicinity of corner ($|x|/s_x\ll 1$) and tips ($|x|/s_x\simeq 0.5$) of the wedge [see Fig. 4(a)]. Inspection of Fig. 4(a) reveals that $\Delta\rho>0$ in the corner while $\Delta\rho<0$ at the tip. The positive deviation indicates that the two walls forming the wedge squeeze the hard spheres into the corner; this effect is more pronounced for smaller values of γ. Around a tip, on the other hand, the hard spheres are spatially less constrained, so that the fluid is more disordered as in the corresponding planar case, so that $\Delta\rho<0$.

Figure 4(b) demonstrates the onset of a modulation of $\Delta\rho(x,z;\gamma)$ along the line of fluid-wall contact which extends slightly into fluid regions further removed from the wall. At planar walls, lateral density oscillations occur only at high bulk densities on account of surface-induced freezing [38]. Because of its corrugation the present substrate facilitates lateral packing effects at values of μ corresponding to considerably lower densities. These lateral oscillations decay

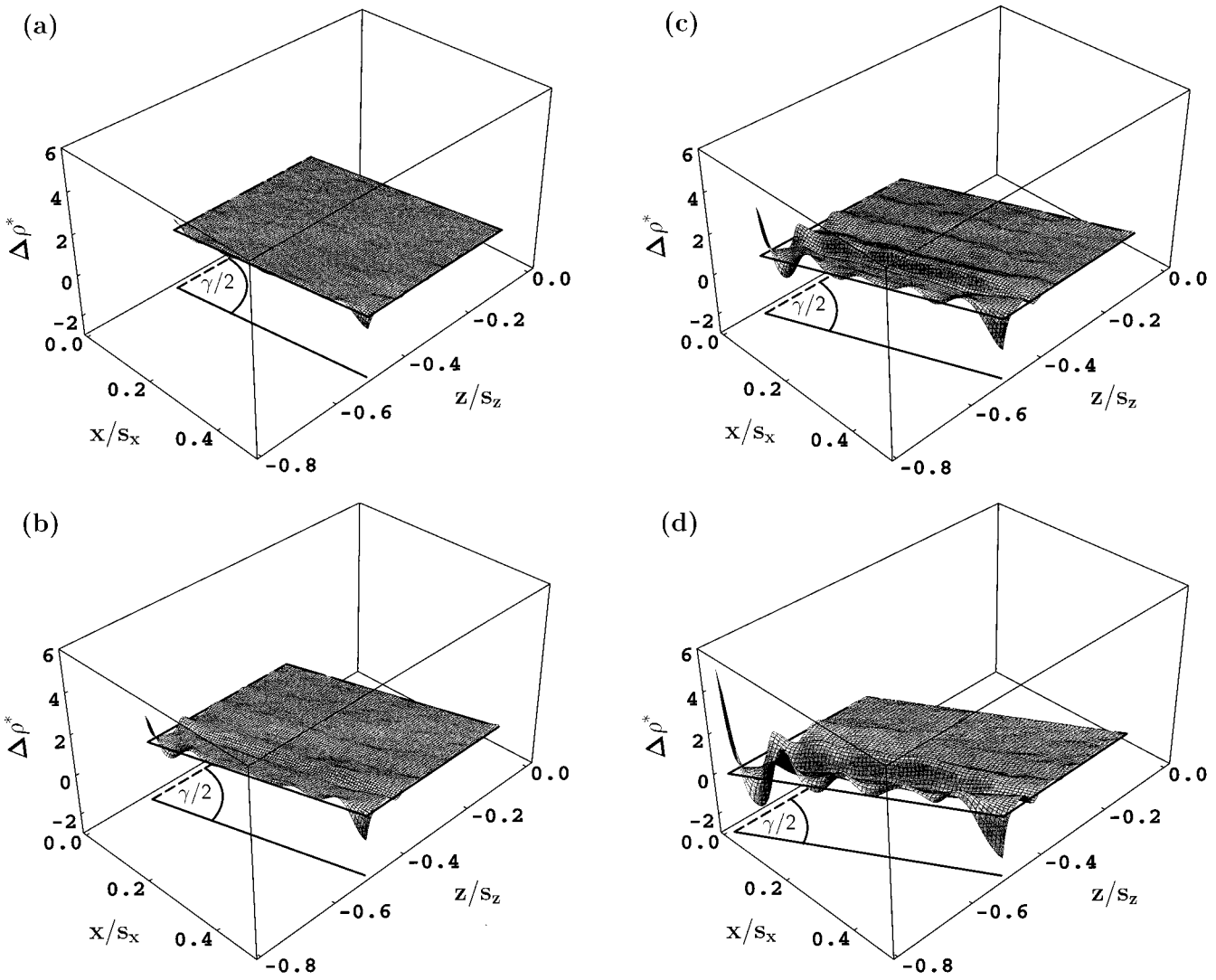

FIG. 4. The deviation $\Delta\rho^*$ of the local density in a wedge of dihedral angle $\gamma=8\pi/9$ (a), $\gamma=7\pi/9$ (b), $\gamma=2\pi/3$ (c), and $\gamma=\pi/2$ (d) from the corresponding local density near a planar hard wall [see Eq. (28)]. The solid line on the bottom of the box indicates the line of fluid-wall contact, $-z_{\mathrm{wall}}(x,\gamma)$ [see Eq. (8)], and the dashed line represents the bisector of the dihedral angle. Because of the symmetry of the system data are shown only for one quadrant $0.0\leqslant x/s_x\leqslant 0.5, -z_{\mathrm{wall}}(x,\gamma)\leqslant z/s_z\leqslant 0.0$, for which the plane $\Delta\rho=0$ is also indicated.

upon moving away from the corner of the wedge toward its tip. In the vicinity of the tip the amplitude of the oscillations in $\Delta\rho(x,z;\gamma)$ increases again. Thus at $\gamma=7\pi/9$, and for the present system size $s_x^*=9.397$, both structural elements (i.e., corner and tip) give rise to localized lateral ordering without strong interference. Therefore, this case resembles closely the behavior of a fluid in a single wedge or at a single tip. For smaller dihedral angles [$\gamma=2\pi/3$ in Fig. 4(c) and $\gamma=\pi/2$ in Fig. 4(d)], packing effects induced by corner and tip merge, so that the oscillations in $\Delta\rho(x,z;\gamma)$ at the fluid-wall contact persist from corner to tip and can no longer be attributed unambiguously to one or the other as in Fig. 4(b). For smaller dihedral angles the lateral extension of packing effects increases together with their amplitude. Both effects lead to more pronounced positive deviations $\Delta\rho(x,z;\gamma)$ (i.e., ''squeezing'') in the corner region. Increasingly negative deviations $\Delta\rho(x,z;\gamma)$ in the tip regime, on the other hand, reflect the more disordered character of the fluid as the tip sharpens with decreasing γ. That the effect of ''squeezing'' in the corner is stronger than the impact of the tip can be inferred from Fig. 4(d), where oscillations in $\Delta\rho(x,z;\gamma)$ along the line $x/s_x=0$ extend further into the fluid than along lines $|x|/s_x=0.5$. Along the former line, $\Delta\rho(x,z;\gamma)$ exhibits three distinct maxima, whereas there are two at most along the latter.

Interference of structural order in corner and tip regions can be visualized by introducing

$$\Delta\rho_{\max}(\gamma):=\max_{x,z}|\Delta\rho(x,z;\gamma)|, \tag{29}$$

which permits one to define a set of points $\mathcal{S}$ according to

$$\mathcal{S}=\{(x,z)\in\mathbb{R}^2|\ \ |\Delta\rho(x,z;\gamma)|\geqslant 0.1\Delta\rho_{\max}(\pi/2)\}. \tag{30}$$

This set is plotted in Fig. 5 for dihedral angles $\gamma=8\pi/9$, $7\pi/9$, $2\pi/3$, and $\pi/2$ considered in Fig. 4. The size of the set indicates the extent to which substrate corrugation modifies the local density significantly compared with a planar substrate. The set $\mathcal{S}$ also allows one to visualize regions where the strongest modifications of $\rho(x,z;\gamma)$ are localized. The

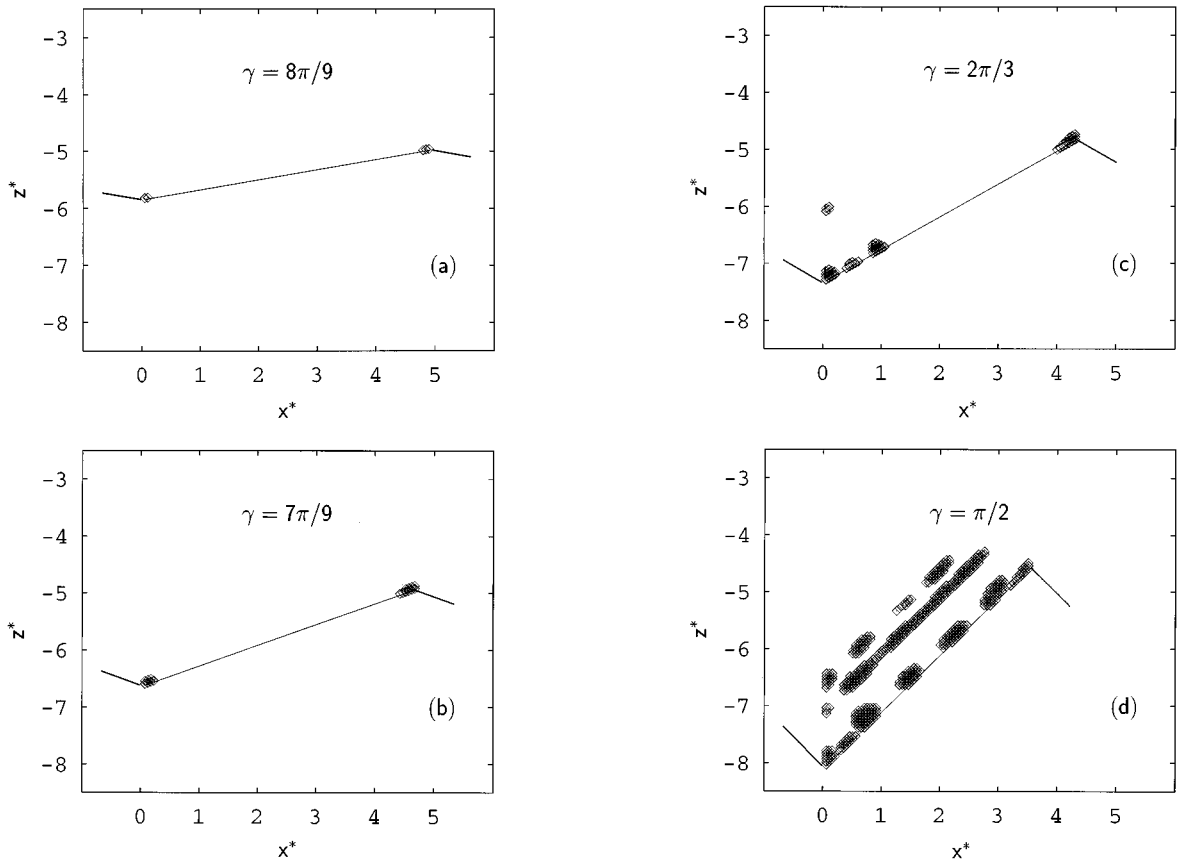

FIG. 5. The set of points $\mathcal{S}$ ($\diamond$) defined in Eqs. (29) and (30) for the same dihedral angles as in Fig. 4. The solid line indicates the line of fluid-wall contact. Within the set $\mathcal{S}$ the deviation of the local density from its planar counterpart is larger than 10% of the maximum deviation for $\gamma=\pi/2$.

sequence of plots in Fig. 5 shows that for sufficiently large values of γ these spatial regions are isolated and located in the neighborhood of corner and tip. As γ decreases, both portions of $\mathcal{S}$ grow in size until they merge. Regions off the wedge wall eventually become a part of $\mathcal{S}$, too. One should keep in mind, however, that because of the absence of attractive interactions the set $\mathcal{S}$ summarizes the purely geometric and entropic effects of confining fluids to corners and tips.

Even though the plots in Fig. 5 demonstrate that for smaller values of γ deviations of the local density from that in front of a planar wall become more important, isodensity lines remain remarkably parallel to the walls. This can be seen in Fig. 6, where the positions of successive extrema of $\rho(x,z;\gamma)$ are plotted. Lines connect points (x,z) pertaining to the location of the same extremum relative to the one at fluid-wall contact; along these lines the values of the extrema vary as functions of x. However, alignment of the extrema with the wall is not perfect, which is particularly evident from Fig. 6(a) referring to $\gamma=\pi/2$. The region over which the nth extrema appear along a line nearly parallel to the wall is shorter if that extremum is further removed from the wall. In the vicinity of a tip (i.e., $|x^*|\rightarrow 3.5$) the regular spacing between successive extrema breaks down reflecting the loss of order in the fluid caused by the sharpness of the tip. Another indicator of disorder near a tip is the lack of localization of higher-order extrema. In particular, the line connecting locations of the third maxima appears to be quite dislocalized for $|x^*|\geqslant 2$, because these maxima are already quite shallow in the tip regime.

The plot in Fig. 6(a) also reveals a peculiar arrangement of hard spheres in the corner of the wedge caused by its tightness. The most favorable configuration is depicted in the inset of Fig. 6(a). One sphere is located in the corner of the wedge in contact with its two sides. The next three spheres are in contact with the first such that the centers of all four spheres form a square in the (x,z) plane whose sides are parallel to the walls of the wedge. Employing the same coordinate system as in Fig. 1, the nearest neighbor of the lowest sphere in the corner along the line $x^*=0$ is then separated from the latter by a distance $\Delta z^*=\sqrt{2}$. These considerations lead to the expectation that successive maxima in the cut $\rho(x=0,z;\gamma=\pi/2)$ are separated by $\Delta z^*\simeq\sqrt{2}$. This is confirmed by the plot in Fig. 6(a). The shift in position of the first minimum to smaller values of z along the line $x^*\simeq 0.5$, as shown by Fig. 6(a), can also be apprehended by the arrangement of spheres described above, and is reflected directly in the plot of the cut $\rho(x^*=0.36,z;\pi/2)$ in Fig. 7, which shows that successive maxima along the line $x^*=0.36$ are not separated by $\Delta z^*\simeq 1.0$ as in the case of planar walls because of the peculiar square packing in the wedge corner described above. It is also interesting to note that the second maximum in $\rho(x^*=0.36,z;\pi/2)$ is smaller than all other maxima, and even smaller than the bulk density which is approached for sufficiently large values of z.

If, on the other hand, the wedge is less tight and the tip at $|x|/s_x=0.5$ is less sharp, the fluid is appreciably more regu-

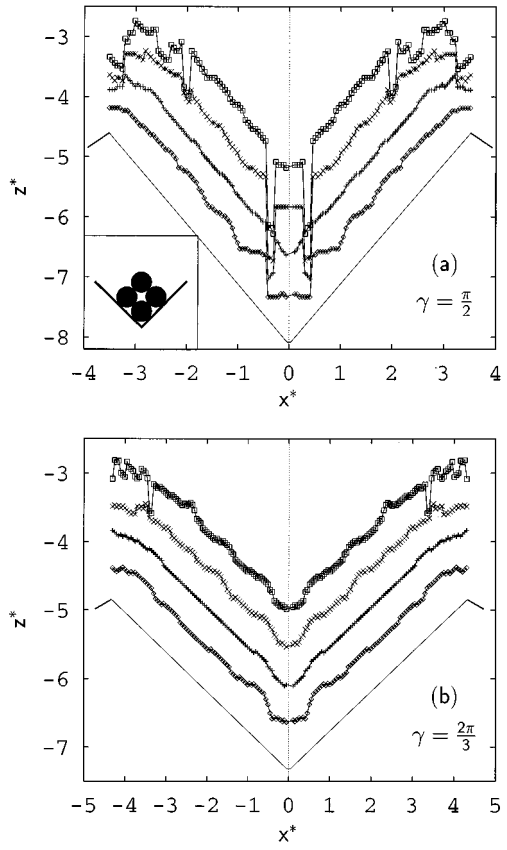

FIG. 6. Positions of successive extrema of $\rho(x,z;\gamma)$ for two selcted dihedral angles $\gamma=\pi/2$ (a) and $\gamma=2\pi/3$ (b); ($\diamond$): first minimum; (+): second maximum; (X): second minimum; ($\square$): third maximum. Lines are intended to guide the eye. The lowest straight lines indicate the position of the line of fluid-wall contact $-z_{\mathrm{wall}}(x;\gamma)$ where the first maximum is attained. The inset in (a) gives the most probable configuration of hard spheres in the corner of the wedge; the positions of the centers of the spheres in this configuration are in accordance with positions of extrema of $\rho(x,z;\gamma)$ (see also Fig. 7). In the inset the line of fluid-wall contact is also indicated.

larly ordered, as one infers from the plot in Fig. 6(b), which shows that for $\gamma=2\pi/3$ the line connecting positions of the second minima stays nearly parallel to the wall over a much larger range compared with its counterpart for $\gamma=\pi/2$ discussed above. The more ordered structure of the fluid in the vicinity of the tip ($x^*\simeq 4.2$) is also reflected by the reduced scatter of points representing the locations of the third maxima, which indicates that these extrema are well-defined and localized even though $\gamma=2\pi/3$ is not so much larger than $\pi/2$ in Fig. 6(a). There is no evidence of a peculiar structure such as the one displayed in Fig. 6(a), so that we conclude that packing of hard spheres in a wedge of $\gamma=\pi/2$ is a geometrically distinguished case.

An even more detailed picture of the structure of a hard-sphere fluid in a hard wedge emerges if one displays $\rho(x,z;\gamma)$ in terms of contour plots which are shown in Fig. 8 for dihedral angles $\gamma=\pi/2$, $2\pi/3$, and π. For the smallest angle $\gamma=\pi/2$, the plot in Fig. 8(a) elucidates structural features discussed in conjunction with Fig. 6(a). For example, from the analysis of Fig. 6(a) a second maximum of $\rho(x,z;\gamma=\pi/2)$ is expected at a distance $\Delta z^*\simeq\sqrt{2}$ from the

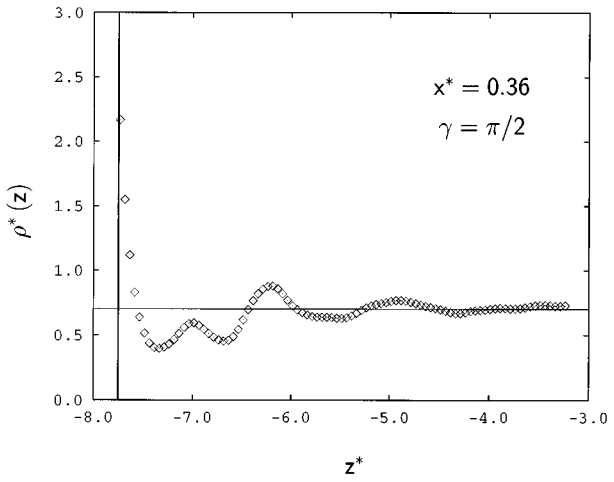

FIG. 7. A cut through the density distribution $\rho(x,z;\gamma)$ along the line $x^*=0.36$ as a function of z^* for $\gamma=\pi/2$. The horizontal line represents the bulk density $\rho_b^*=0.7016$, and the vertical line indicates the position of the point of fluid-wall contact.

point at which the fluid is in contact with the wall along the line $x^*=0$. In the corresponding plot in Fig. 8(a), this second maximum of $\rho(x,z;\gamma=\pi/2)$ is represented by a density ''island'' centered at $x^*=0$, and surrounded by a line along which $\rho^*(x,z;\gamma=\pi/2)=1.0$. That this line encloses second maxima of $\rho(x,z;\gamma=\pi/2)$ is inferred from the same distance $\Delta z^*\simeq\sqrt{2}$ from the point of fluid-wall contact at which the island in the plot of Fig. 8(a) arises. The contour plot also shows that the first minimum centered at $x^*=0$ and represented by a closed line along which $\rho^*(x,z;\pi/2)=0.1$ appears halfway in between the point of fluid-wall contact, and the the second maximum as expected for geometric reasons. In the x direction the second maxima appear to be framed by two minima separated from the former by a distance of $\Delta x^*\simeq 0.5$, which supports the configuration depicted in the inset of Fig. 6(a).

However, as can be seen from Fig. 8(b), for $\gamma=2\pi/3$ typical configurations in the wedge are distinct from the one displayed in Fig. 6(a). The two minima framing the second maxima in Fig. 8(a) are missing, and the isodensity lines are nearly parallel to the wall over a range $0.5<x^*\leqslant 3.5$, i.e., away from the close vicinity of tip or corner. The influence of the tip on hard-sphere packing results in the tendency of isodensity lines to become more parallel to the x axis as $x^*\rightarrow 4.33$, indicating a less structured fluid. Because of the enhanced sharpness of the tip at $\gamma=\pi/2$, this trend is more pronounced in Fig. 8(a). The corner, on the other hand, causes the fluid to be more ordered, as revealed by the succession of ''islands'' along the line $x^*\simeq 0$ in Fig. 8(b) representing successive minima and maxima of $\rho(x,z;\gamma)$, which extend further into the fluid than along any other line of $x=\mathrm{const}$.

Finally, in the special case of planar walls the local density must be independent of x as long as there is no surface-induced freezing. The contour plot of $\rho(x,z;\pi)$ in Fig. 8(c) shows that the isodensity lines indeed run parallel to the wall. Disconnected isodensity lines enclosing the second maxima of $\rho(x,z;\gamma=\pi)$ in the vicinity of $z^*\simeq 4.0$ are caused by statistical noise, and are not a signature of physically relevant structures.

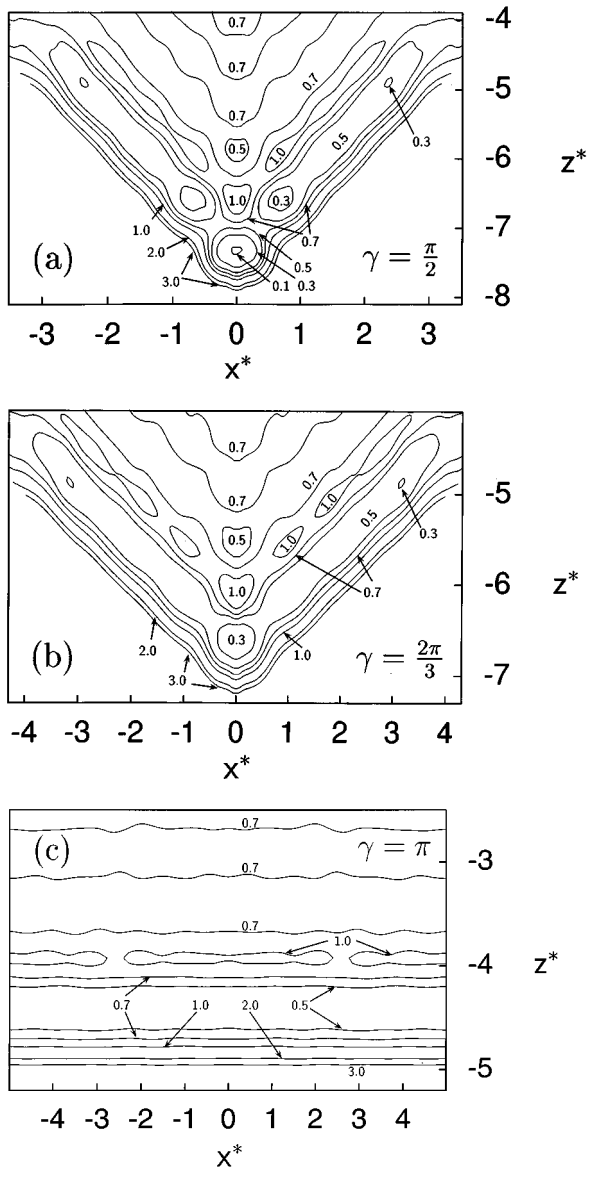

FIG. 8. Contour plots of $\rho(x,z;\gamma)$ for three selected dihedral angles $\gamma=\pi/2$ (a), $\gamma=2\pi/3$ (b), and $\gamma=\pi$ (c). Numbers and arrows are inserted to identify the various lines of constant $\rho^*(x,z;\gamma)$. For reasons of clarity the lines of fluid-wall contact are not shown.

C. Adsorption

Experimentally, the determination of the full local-density distribution near microstructured substrates is rather challenging. As a first step one frequently focuses on a reduced, integral description of the inhomogeneous fluid by measuring the excess coverage Γ using, say, volumetric techniques (see, e.g., Ref. [39]). For a single substrate of the present periodic system the relation between Γ and the density distribution $\rho(x,z;\gamma)$ is given by (see Fig. 1)

$$\Gamma(\gamma)=2\int_{-s'/2}^{s'/2}dy\int_{-s_x/2}^{0}dx\lim_{s_z\to\infty}\int_{-z_{\rm wall}(x;\gamma)-\sigma/\sin(\gamma/2)}^{0}\times dz[\rho(x,z;\gamma)-\rho_b]. \tag{31}$$

The prefactor 2 reflects the symmetry of the density distribution around the $x-y$ plane. The lower limit of the third integral is the position of the lower wall of the wedge defined in Eq. (8). The first integral yields a factor of s' for the linear extension of the system in the y direction. For an array of M parallel grooves the total excess coverage $\Gamma_{\rm tot}$ is given by $\Gamma_{\rm tot}=M\Gamma(\gamma)$.

In the thermodynamic limit $s'\to\infty$, which also implies $s_x\to\infty$ [see Eq. (1)], the excess coverage $\Gamma(\gamma)$ within a unit cell contains a so-called surface contribution Γ_s which scales with the actual area s'^2 of the walls forming the groove and a so-called line contribution Γ_l which scales with the linear extension s' in the translationally invariant y direction. While Γ_s is solely determined by the density profile $\rho[x,z+z_{\rm wall}(x;\gamma);\gamma=\pi]\equiv\rho(z)$ of a semiinfinite fluid exposed to a flat substrate, the line contribution arises because of the deviation of the local density caused by corner and tip from that at a planar substrate. On the basis of Fig. 1, one finds the following decomposition in the thermodynamic limit $s'\to\infty$:

$$\Gamma(\gamma)=\Gamma_s+\Gamma_l+O[(s')^0], \tag{32}$$

with

$$\Gamma_s=s'^2\int_0^\infty[\rho(z)-\rho_b]dz \tag{33}$$

and

$$\Gamma_l=-2s'\cot\frac{\gamma}{2}\int_0^\infty z[\rho(z)-\rho_b]dz+\Gamma_l^{\rm tip}+\Gamma_l^{\rm corner}, \tag{34}$$

where

$$\Gamma_l^{\rm tip}=2s'\int_0^\infty d\tilde{x}\int_0^\infty\left[\rho_{\rm tip}(\tilde{x},\tilde{z};\gamma)-\rho\left(\tilde{z}+\tilde{x}\cot\frac{\gamma}{2}\right)\right]d\tilde{z}+2s'\int_0^\infty d\tilde{x}\int_{-\tilde{x}\cot(\gamma/2)}^0[\rho_{\rm tip}(\tilde{x},\tilde{z};\gamma)-\rho(\mathcal{Z})]d\tilde{z} \tag{35}$$

and

$$\Gamma_l^{\rm corner}=2s'\int_0^\infty dx'\int_{x'\cot(\gamma/2)}^\infty[\rho_{\rm corner}(x',z';\gamma)-\rho(\mathcal{Z})]dz'. \tag{36}$$

In Eq. (33), s'^2 is the area of the walls forming a single groove, and $\rho(z)$ is the density profile in front of a planar substrate with fluid-wall contact at $z=\sigma$. This implies the relation $\Gamma(\gamma=\pi)=\Gamma_s$. For $s'\to\infty$ the distance $s_x=s'\sin(\gamma/2)$ between neighboring tips and the depth $D=(s'/2)\cot(\gamma/2)$ of the groove become macroscopically large. Therefore, in this limit $\rho(x,z;\gamma)$ decomposes into a density distribution $\rho_{\rm tip}(\tilde{x},\tilde{z};\gamma)$ around the tip $(\tilde{x}=0,\tilde{z}=0)$, where $\tilde{x}=x+s_x/2$ and $\tilde{z}=z+s_z/2$ (see Fig. 1) and a density distribution $\rho_{\rm corner}(x',z';\gamma)$ in the corner where $x'=x$ and $z'=z+D+s_z/2$. These two density distributions are separated by the density distribution $\rho(\mathcal{Z})$ of a fluid near a flat wall where $\mathcal{Z}$ is the normal distance from the wall (see Fig. 1). In the present case one has

$\mathcal{Z}=\tilde{z}\sin(\gamma/2)+\tilde{x}\cos(\gamma/2)$ and $\mathcal{Z}=z'\sin(\gamma/2)-x'\cos(\gamma/2)$, respectively. Since in the thermodynamic limit $s'\to\infty$, the neighboring tips as well as a tip and the corner are macroscopically far apart, $\rho_{\rm tip}(\tilde{x}\to\infty,\tilde{z};\gamma)$ and $\rho_{\rm corner}(x'\to\infty,z';\gamma)\to\rho(\mathcal{Z})$. The same behavior is encountered if both $\tilde{x}$ and $\tilde{z}$ or x' and z' become large simultaneously, such that one moves in a direction parallel to the walls of the grooves. This guarantees that the second term in Eq. (35) as well as Eq. (36) are indeed finite. The first term in Eq. (35) takes into account that the density distribution above the tip approaches the density profile $\rho(u)$ of the planar geometry with the argument $u=\tilde{z}+\tilde{x}\cot(\gamma/2)$ given by the vertical distance of the point $(\tilde{x},\tilde{z})$ from the tip at $\tilde{z}=-\tilde{x}\cot(\gamma/2)$. The integrand of this term vanishes if $\tilde{x}$ or $\tilde{z}$ are large in any direction. Therefore, $\Gamma_l^{\rm tip}$ and $\Gamma_l^{\rm corner}$ are indeed line contributions proportional to s'. The first term in Eq. (34) represents a third line contribution which arises because the density profiles $\rho[\tilde{z}+\tilde{x}\cot(\gamma/2)]$ and $\rho(\mathcal{Z})$ are subtracted in Eqs. (35) and (36) respectively, instead of ρ_b as in Eq. (31). In the limit $\gamma\to\pi$ all three terms in Eq. (34) vanish in accordance with the relation $\Gamma(\gamma=\pi)=\Gamma_s$.

For the special case of a planar substrate we obtain $\Gamma^*(\gamma=\pi)=\Gamma_s^*=-49.4$ from Eq. (31), a value which deviates only by about 4% from $\Gamma^*(\gamma=\pi)=-47.6$ obtained in Ref. [40] from a density-functional calculation for the present thermodynamic state. Almost perfect agreement is achieved with numbers from both molecular dynamics [41] and scaled particle theory [42] which give $\Gamma^*(\gamma=\pi)=-49.67$ [see Fig. 3 in Ref. [40]; note that our definition of $\Gamma(\gamma=\pi)$ deviates from the one used in Ref. [40] by a factor of s'^2 because of the additional integrations over x and y in Eq. (31)]. The integral in the first term on the right-hand side of Eq. (34), yielding the first moment of the density profile, is also amenable to a density-functional calculation which gives a value of 0.23–0.25 depending on the specific version of the density-functional used [43]. From the present GCEMC simulations we obtain a value of 0.17. In view of the fact that the first moment of the density profile enhances the relative weight of details of the oscillatory decay of the profile compared with the zeroth moment, we also regard this as satisfactory agreement.

Given the present system size $\Gamma_l^{\rm tip}$ and $\Gamma_l^{\rm corner}$ in Eqs. (35) and (36) cannot be computed independently because of the structural interference of tips and corner discussed in Sec. III A. The latter prevents a direct determination of either $\rho_{\rm tip}$ or $\rho_{\rm corner}$. However, *via* Eqs. (32)–(34) the sum $(\Gamma_l^{\rm tip}+\Gamma_l^{\rm corner})/s'+O(1/s')$ can be computed from the density profiles obtained in GCEMC simulations. Results plotted in Fig. 9 show that in accordance with its definition in Eq. (32) the sum vanishes if the substrate is planar. With decreasing γ the sum increases reflecting the growing importance of substrate corrugation on the adsorption of hard spheres in grooves.

IV. SUMMARY AND DISCUSSION

We investigated the density distribution in a fluid of hard spheres of diameter σ exposed to a periodically corrugated, hard substrate which is characterized by its dihedral angle γ and the depth D of the grooves (see Fig. 1). Based upon GCEMC simulations, we studied the variation of structural properties of the fluid as functions of γ over the range $\pi/2\leqslant\gamma\leqslant\pi$; for $\gamma=\pi$ the substrate is flat. Our main findings are the following:

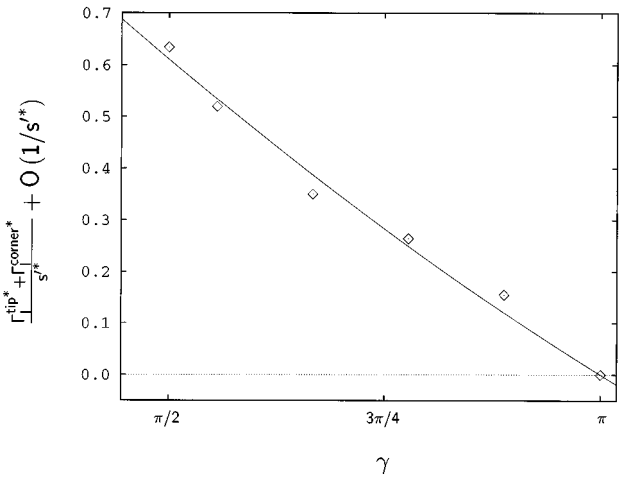

FIG. 9. $(\Gamma_l^{\rm tip*}+\Gamma^{\rm corner*})/s'^*+O(1/s'^*)$ as a function of the dihedral angle γ which is a measure of the influence of lateral corrugation of the walls on adsorption (see main text). The solid line represents a fit to the data points ($\diamond$) intended to guide the eye.

(1) GCEMC simulations can be carried out successfully and reliably for this confined system characterized exclusively by hard-core interactions (see Fig. 2). The pronounced statistical fluctuations require the application of a smoothing procedure to the Monte Carlo data. Figures 2 and 3 demonstrate the reliability of the smoothing algorithm.

(2) Corner and tips of wedges have opposite effects on the packing of fluid molecules in front of the substrate. While the fluid is more ordered in a corner, less order is observed at tips compared with a corresponding planar wall. This difference increases in tighter wedges with sharper tips (see Fig. 4).

(3) Lateral and normal extension of regions over which corner and tips affect the packing of fluid molecules depend on γ. For a given depth D, specific packing effects close to the tip and deep in the corner, respectively, start to interfere with decreasing γ. In the present simulations this interference sets in for $\gamma\leqslant 2\pi/3$ and $D^*=2.5$ (see Fig. 5).

(4) In the thermodynamic limit $D\gg\sigma$, $\Gamma(\gamma)$ decomposes into a surface contribution Γ_s proportional to the actual surface area of the corrugated substrate and into a line contribution $\Gamma_l(\gamma)$ proportional to the linear extension of the grooves in the direction normal to the lateral corrugation [see Eqs. (34)–(36)].

(5) The line contribution $\Gamma_l(\gamma)$, which vanishes for the special case of a planar substrate, increases with decreasing γ, indicating the importance of substrate corrugation for the adsorption of fluids at nonplanar substrates (see Fig. 9). While the line contribution Γ_l is negative, the surface contribution, which agrees well with previous work [40–42], is positive. Although Γ_l is subdominant to Γ_s, this shows that the corrugation of a substrate weakens the negative net adsorption on a flat substrate.

For a single rectangular corner, Nijmeijer and van Leeu-

wen [44] derived a sum rule which expresses the integral over the deviation of the density at contact with the walls of the wedge from the corresponding contact value at a flat surface in terms of the wall-fluid interfacial tension σ_{wf} of a hard-sphere fluid at a flat hard wall [see Eq. (36)]:

$$\int_0^\infty \left[\rho_{\text{corner}}\left(x', z' = x'; \gamma = \frac{\pi}{2} \right) - \rho(\mathcal{Z} = 0) \right] dx' = -\beta \sigma_{wf} \sigma^2. \tag{37}$$

We tried to check whether our GCEMC data fulfill this exact sum rule. First, we found that $\rho(x', z' = x'; \gamma = \pi/2)$ exhibits pronounced oscillations as a function of x' for x' close to the center of the corner. However, for the presently accessible system sizes it turned out that the influence of the tip at the upper end of the wedge sets in before the asymptotic value $\lim_{x' \to \infty} \rho_{\text{corner}}(x', z' = x'; \gamma = \pi/2) = \rho(\mathcal{Z} = 0)$ is reached so that the effect of a single corner cannot be isolated with sufficient precision. To study this interference effect on the above sum rule [see Eq. (36)] we analyzed the integral

$$I(x) = \int_0^x \left[\rho\left(x', z' = x'; \gamma = \frac{\pi}{2} \right) - \rho(\mathcal{Z} = 0) \right] dx'. \tag{38}$$

Within the range $0.0 \leqslant x/s_x \leqslant 0.3$, $I(x)$ exhibits a damped oscillatory behavior around a value of approximately 0.94. This number turns out to be rather close to the value $-\beta \sigma_{wf} \sigma^2 = 1.0$ predicted in Ref. [36] for the current thermodynamic state. For larger values of x, i.e., $0.3 \leqslant x/s_x \leqslant 0.5$, the oscillations in $I(x)$ become more pronounced because of the onset of the tip influence. From these observations we conclude that finite-size effects are more severe for the local-density distribution than for integral quantities such as the left-hand side of Eq. (37). This observation is in line with those for the excess coverage $\Gamma(\gamma)$ (see Sec. III C).

Finally, we would like to mention that we obtained $\rho(x, z; \gamma)$ by averaging the local-density distribution over the y direction in which the sytem is translationally invariant. However, it would be interesting to resolve the density distribution in this direction to test whether the fluid at the bottom of the groove starts to exhibit solidlike structures which would be signaled by a periodic density variation in the y direction. However, one should keep in mind that in spatial dimensions $d = 1$ and 2 there is no true long-range order. Nonetheless, in $d = 2$ one expects a Kosterlitz-Thouless type of phase transition to occur at a specific critical density ρ_c, so that, for densities $\rho < \rho_c$, a phase exists which is characterized by exponentially decaying correlation functions, while for $\rho > \rho_c$ these correlation functions decay according to a power law; in $d = 1$ there is no phase transition up to close packing. However, this expectation has not yet been established explicitly, either experimentally or by simulations. What one does find is, that in $d = 2$ finite-size systems exhibit a (*quasi*)-first-order transition to a structure resembling very closely a solid phase; only in the thermodynamic limit this solidlike structure is expected to be replaced by a Kosterlitz-Thouless phase. Since in $d = 1$ the finite extension of a system also leads to a slower decay of oscillations in the pair correlation function, it would be interesting to see whether the one-dimensional grooves of the present substrate enhance the formation of the aforementioned solidlike structure in a *quasi*-two-dimensional film near the substrate so that the (*quasi*)-first-order phase transition occurs at a lower density than the substrate-induced (*quasi*)freezing at a flat wall which was observed in Ref. [38] only at much higher densities than the one studied here.

ACKNOWLEDGMENTS

We thank Bernd Götzelmann (Bergische Universität Wuppertal) for helpful discussions and for providing unpublished data. Thomas Gruhn (Technische Universität Berlin) is acknowledged for preparing the plots presented in this work. One of us (M.S.) is indebted to the Deutsche Forschungsgemeinschaft (DFG) for financial support.

[1] C. L. Rhykerd, Jr., M. Schoen, D. J. Diestler, and J. H. Cushman, Nature (London) **330**, 461 (1989).
[2] M. Schoen, *Computer Simulation of Condensed Phases in Complex Geometries* (Springer-Verlag, Heidelberg, 1993).
[3] J. S. Rowlinson and B. Widom, *Molecular Theory of Capillarity* (Clarendon, Oxford, 1984).
[4] S. Dietrich, in *Phase Transitions and Critical Phenomena*, edited by C. Domb and J. L. Lebowitz (Academic, London, 1988), Vol. 12, p. 1.
[5] M. Schick, in *Liquides aux Interfaces, Les Houches 1988 Session XLVIII, Course Nine*, edited by J. Charvolin, J. Joanny, and J. Zinn-Justin (North-Holland, Amsterdam, 1990).
[6] *Fundamentals of Inhomogeneous Fluids*, edited by D. Henderson (Dekker, New York, 1992).
[7] R. Evans and M. Chan, Phys. World (1996), 48.
[8] A. Hirtz, K. Bonkhoff, and G. H. Findenegg, Adv. Colloid Interface Sci. **44**, 241 (1993).
[9] H. Dosch, in *Critical Phenomena at Surfaces and Interfaces*, Springer Tracts in Modern Physics (Springer-Verlag, Heidelberg 1992), Vol. 126.
[10] S. Dietrich and A. Haase, Phys. Rep. **260**, 1 (1995).
[11] C. M. Mate, G. M. McClelland, R. Erlandsson, and S. Chiang, Phys. Rev. Lett. **59**, 1942 (1987).
[12] B. Bhushan, J. N. Israelachvili, and U. Landman, Nature (London) **374**, 607 (1995).
[13] P. E. Sheehan and C. M. Lieber, Science **272**, 1158 (1996).
[14] J. N. Israelachvili, *Intermolecular and Surface Forces* (Academic, London, 1992).
[15] D. Beaglehole, J. Chem. Phys. **93**, 893 (1989).
[16] S. Garoff, E. B. Sirota, S. K. Sinha, and H. B. Stanley, J. Chem. Phys. **90**, 7505 (1989).
[17] I. M. Tidswell, T. A. Rabedeau, P. S. Pershan, and S. D. Kosowsky, Phys. Rev. Lett. **66**, 2108 (1991).
[18] P. S. Pershan, Ber. Bunsenges. Phys. Chem. **98**, 372 (1994).
[19] D. Andelman, J.-F. Joanny, and M. O. Robbins, Europhys. Lett. **7**, 731 (1988).

[20] M. O. Robbins, D. Andelman, and J.-F. Joanny, Phys. Rev. A **43**, 4344 (1991).
[21] J. L. Harden and D. Andelman, Langmuir **8**, 2547 (1992).
[22] R. R. Netz and D. Andelman, Phys. Rev. E **55**, 687 (1997).
[23] P. Müller-Buschbaum, M. Tolan, W. Press, F. Brinkop, and J. P. Kotthaus, Ber. Bunsenges. Phys. Chem. **98**, 413 (1994).
[24] M. Napiórkowski, W. Koch, and S. Dietrich, Phys. Rev. A **45**, 5760 (1992).
[25] J. A. Mann, Jr., L. Romero, R. R. Rye, and F. G. Yost, Phys. Rev. E **52**, 3967 (1995).
[26] R. R. Rye, F. G. Yost, and J. A. Mann, Langmuir **12**, 4625 (1996).
[27] R. R. Rye, F. G. Yost, and J. A. Mann, Langmuir **12**, 555 (1996).
[28] B. F. Jones and E. Galan, *Reviews in Mineralogy, Vol. 19: Hydrous Phyllosilicates* (Bookcrafters, Chelsea, 1988).
[29] J. E. Curry, F. Zhang, J. H. Cushman, M. Schoen, and D. J. Diestler, J. Chem. Phys. **101**, 10 824 (1994).
[30] M. P. Allen and D. J. Tildesley, *Computer Simulation of Liquids* (Clarendon, Oxford, 1987).
[31] D. A. McQuarrie, *Statistical Mechanics* (Harper & Row, New York, 1976).
[32] S. A. Rice and P. Gray, *The Statistical Mechanics of Simple Fluids* (Interscience, New York, 1965), Chap. 4.
[33] D. J. Adams, Mol. Phys. **29**, 307 (1975).
[34] N. F. Carnahan and K. E. Starling, J. Chem. Phys. **51**, 635 (1969).
[35] J. P. Hansen and I. R. McDonald, *Theory of Simple Liquids*, 2nd ed. (Academic, London, 1986).
[36] B. Götzelmann and S. Dietrich, Phys. Rev. E **55**, 2993 (1997).
[37] R. W. Hamming, *Numerical Methods for Scientists and Engineers*, 2nd ed. (McGraw-Hill, New York, 1973), Chap. 35.6.
[38] See Figs. 3(a) and 3(c) in D. J. Courtemanche and F. van Swol, Phys. Rev. Lett. **69**, 2078 (1992).
[39] M. Thommes and G. H. Findenegg, Langmuir **10**, 4270 (1994).
[40] B. Götzelmann, A. Haase, and S. Dietrich, Phys. Rev. E **53**, 3456 (1996).
[41] J. R. Henderson and F. van Swol, Mol. Phys. **51**, 991 (1984).
[42] H. Reiss, H. L. Frisch, E. Helfand, and J. L. Lebowitz, J. Chem. Phys. **32**, 119 (1960).
[43] B. Götzelmann (private communication).
[44] A. J. P. Nijmeijer and J. N. J. van Leeuwen, J. Phys. A **23**, 4211 (1990).